

Continuous wavelet transform, theoretical aspects and application to aeromagnetic data at the Huanghua Depression, Dagang Oilfield, China

Yushan Yang*, Yuanyuan Li and Tianyou Liu

Institute of Geophysics and Geomatics, China University of Geosciences, Lumo Street 485, Wuhan, HuBei 430074, China

Received September 2008, revision accepted September 2009

ABSTRACT

We use the continuous wavelet transform based on complex Morlet wavelets, which has been developed to estimate the source distribution of potential fields. For magnetic anomalies of adjacent sources, they always superimpose upon each other in space and wavenumber, making the identification of magnetic sources problematic. Therefore, a scale normalization factor, a^{-n} , is introduced on the wavelet coefficients to improve resolution in the scalogram. By theoretical modelling, we set up an approximate linear relationship between the pseudo-wavenumber and source depth. The influences of background field, random noise and magnetization inclination on the continuous wavelet transform of magnetic anomalies are also discussed and compared with the short-time Fourier transform results.

Synthetic examples indicate that the regional trend has little effect on our method, while the influence of random noise is mainly imposed on shallower sources with higher wavenumbers. The source horizontal position will be affected by the change of magnetization direction, whereas the source depth remains unchanged. After discussing the performance of our method by showing the results of various synthetic tests, we use this method on the aeromagnetic data of the Huanghua depression in central China to define the distribution of volcanic rocks. The spectrum slices in different scales are used to determine horizontal positions of volcanic rocks and their source depths are estimated from the modulus maxima of complex coefficients, which is in good accordance with drilling results.

INTRODUCTION

Increasing depletion of hydrocarbon reserves in traditional oilfields shifted focus toward more volcanic basins (Schutter 2003). Major exploration successes have been achieved in many countries, such as the USA, Georgia, Germany, Indonesia, Argentina, Mexico, Brazil, Russia, etc., especially in the Niigata Basin of Japan, with the discovery of Yoshii – East Kashiwazaki gas fields in the early 1990s (Hunter and Davies 1979; Mitsuata, Matsuo and Minegishi

1999). China has also witnessed great achievements in volcanic reservoir exploration in the Huanghua, Junggar and Songliao basins (Luo, Zhang and Qu 1999). However, although widely distributed, volcanic reservoirs are generally in small scales with diversified lithofacies and complex reservoir forming conditions, which is a major hurdle for the follow-up success in seismic exploration.

By contrast, magnetic data are useful for interpretation in igneous basins, especially when other methods such as seismic data are less reliable. Volcanic rocks commonly show a strong magnetic signal because of their high magnetic minerals content (Emeleus and Bell 2005). High wavenumber anomalies are commonly characteristic of shallow igneous intrusions,

*E-mail: samyys@126.com

whereas the same intrusions covered by thick basins produce less obvious, lower wavenumber anomalies. To identify them, spectral analysis is usually adopted on magnetic grids (Spector and Grant 1970; Bhattacharyya and Leu 1975).

Various techniques have been developed for the spectral decomposition of geophysical data (Peyton, Bottjer and Partyka 1998; Partyka, Gridley and Lopez 1999; Hardy, Richard and Gaston 2003; Castagna, Sun and Siegfried 2003; Sinha *et al.* 2005; Castagna and Sun 2006; Kazemeini *et al.* 2007, 2009). As a traditional frequency decomposition method, the discrete Fourier transform is not suitable for analysis of non-stationary signals since it is unable to localize frequency variations over time (Moreau *et al.* 1997; Fedi *et al.* 1998; Hornby, Boschetti and Horowitz 1999). To handle this problem, the short time Fourier transform method is widely used for the decomposition of non-stationary signals (Cohen 1995). One problem with this approach is that the fixed width 'window function' results in limited resolution. The continuous wavelet transform can be used as an alternative approach to overcome this resolution problem (Moreau *et al.* 1999; Sailhac *et al.* 2000; Sinha *et al.* 2005). In the continuous wavelet transform, the signal is multiplied with a wavelet function similar to a 'window function' but the width of the window is not fixed. The time window width is allowed to vary depending upon the frequency that is being considered.

The use of continuous wavelet transforms was introduced in the analysis of potential fields by Moreau (1997), who analysed the potential field anomaly due to isolated sources and showed that the maxima lines of the continuous wavelet transform converge where the source is located. Moreover, isolated anomalies due to a single homogeneous body of simple geometrical shape may also be studied using a best depth estimation technique (Moreau *et al.* 1999), or parametric curves of wavelet maxima location and amplitude versus the scale parameter a (Hornby *et al.* 1999). Sources such as vertical and dipping magnetized prisms may be more conveniently analysed by a complex continuous wavelet transform (Sailhac *et al.* 2000; Martelet *et al.* 2001), using the modulus of the continuous wavelet transform to estimate the source thickness and its phase for the dip.

In real cases potential field anomalies are, however, the superposition of several components, related to sources belonging to different positions, extents and depths. This appears to be a major problem for the identification of volcanic rocks in the case of strong interference. In this case, the maxima associated with larger anomalies in the scalograms of wavelet coefficients modulus are often dominating those associated with smaller anomalies, making the identification of magnetic

sources problematic. To overcome the aforementioned problems, we devised a scale normalization scheme to amplify the wavenumber gaps of various anomalies, thus facilitating the identification of magnetic sources in strong interference. For a better delineation of source depths, a linear relationship between the source depth and the wavelet pseudo-wavenumber is developed in our synthetic example. Then we demonstrate the effects of background magnetic field, random noise and the magnetization inclination on the modelling results. After discussing the performance of our method on various source types, we adopt this method on the aeromagnetic data of the Huanghua depression in central China to define their source distribution.

THE METHODOLOGY

The continuous wavelet transform

Let us briefly review the main concepts of continuous wavelet transform. For any 1D signal $s \in L^2(R)$, its continuous wavelet transform, \tilde{S}_W is defined as the integral transform (Mallat 1999)

$$\tilde{S}_W(a, b) = \int_{-\infty}^{\infty} s(x) \frac{1}{\sqrt{a}} \bar{\psi} \left(\frac{x-b}{a} \right) dx, \quad (1)$$

where $\bar{\psi}$ is the complex conjugate of a fixed function $\psi \in L^2(R)$, called the mother wavelet or analysing wavelet; $a \in R^+$ and $b \in R$, are the scale (or the dilation) and the translation parameter, respectively, with R^+ being the set of positive real numbers. $L^2(R)$ denotes the Hilbert space of square integrable functions. $\tilde{S}_W(a, b)$ is the scalogram (wavelet coefficients). The convolution integral in equation (1) can be computed easily in the Fourier domain. The choice for the scale and the translation parameter can be arbitrary and we can choose to represent them any way we like.

In practice, small scales imply a high space resolution, while the converse is true for large scales (Daubechies 1987). This is obviously different from the Fourier transform, where the space resolution is absent for any given wavenumber but also from the windowed Fourier transform (Gabor 1946), where constant widths are assumed for wavenumber band and spatial width. Hence the flexibility of wavelets is optimal for studying non-stationary signals having high wavenumber signals superposed on low wavenumber signals.

For a 2D signal $s(x, y)$, its continuous wavelet transform is defined as

$$\tilde{S}_W(a, b_x, b_y) = \frac{1}{a} \int_{-\infty}^{\infty} \int_{-\infty}^{\infty} s(x, y) \bar{\psi} \left(\frac{x-b_x}{a}, \frac{y-b_y}{a} \right) dx dy, \quad (2)$$

where $\psi(x, y)$ is the 2D mother wavelet and b_x and b_y are translation parameters in the x and y direction. If $\psi(x, y) = \psi(x) \psi(y)$, equation (2) can be transformed into

$$\tilde{S}_W(a, b_x, b_y) = \int_{-\infty}^{\infty} \left[\int_{-\infty}^{\infty} s(x, y) \frac{1}{\sqrt{a}} \tilde{\psi} \left(\frac{x - b_x}{a} \right) dx \right] \times \frac{1}{\sqrt{a}} \tilde{\psi} \left(\frac{y - b_y}{a} \right) dy. \quad (3)$$

Therefore, equation (3) can be fulfilled by applying the 1D continuous wavelet transform in the x - and y -directions separately. The magnetic data will be transformed into three-dimensional, in which the source information in different depths can be obtained by analysing the wavelet spectrum in different scales.

Complex wavelets

An important step in continuous wavelet transform is selecting the 'wavelet function', also known as the 'mother wavelet'. Complex wavelets can easily be constructed from real wavelets through the Hilbert transform (Pascal 2000). There are four kinds of commonly-used complex wavelets: complex Morlet wavelets, complex Gaussian wavelets, complex frequency B-spline wavelets and complex Shannon wavelets. Among them, the complex Morlet wavelets, whose Fourier transform is a Gaussian function, are a fairly ideal band-pass filter. Therefore, it is adopted in our work for the signal amplitude analysis.

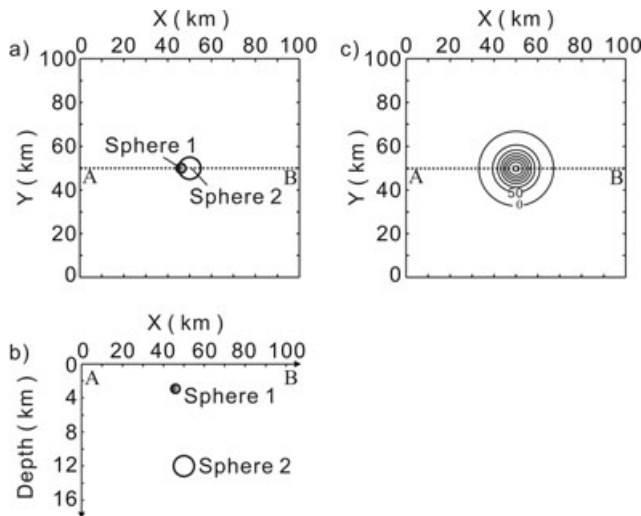


Figure 1 Synthetic model. a) Plane view from above, b) A-B profile map across sphere centres, c) total magnetic intensity anomalies (unit: nT). Profile A-B (dashed line) passes through sphere centres.

The complex Morlet mother wavelet is defined as:

$$\psi(x) = \sqrt{\pi k_b} e^{(-x^2/k_b + 2i\pi k_{c,w}x)}, \quad (4)$$

where k_b is the bandwidth parameter and $k_{c,w}$ is the wavelet centre wavenumber. By dilating and translating this wavelet $\psi(x)$, we produce a family of wavelets:

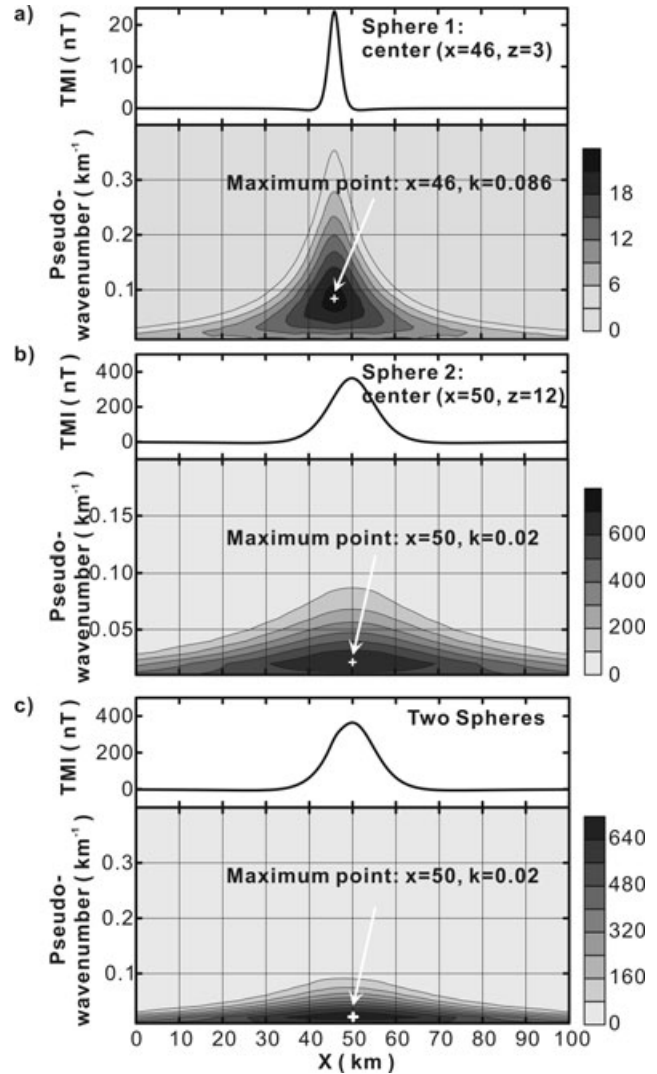


Figure 2 TMI anomalies on profile A-B and their scalograms. The complex Morlet wavelet (cmor1-1, bandwidth $k_b = 1 \text{ km}^{-1}$, centre wavenumber $k_{c,w} = 1 \text{ km}^{-1}$) is used as the analysing wavelet. Contours and scale bars show the dimensionless modulus of wavelet coefficients. The pseudo-wavenumbers k_a is calculated from equation (5). The modulus maxima are labelled as white plus. a) total magnetic intensity anomalies (top) and their scalogram (bottom) caused by single sphere 1, b) total magnetic intensity anomalies (top) and their scalogram (bottom) caused by single sphere 2 and c) by two spheres.

$$\psi_{a,b}(x) = \frac{1}{\sqrt{a}} \psi\left(\frac{x-b}{a}\right). \quad (5)$$

Due to the complex feature of the wavelet coefficients generated by the complex Morlet wavelet, we actually computed the modulus of the complex scalogram in the spectrum analysis.

The relationship between scale and wavenumber

We note that a scale represents a range of depth or a wavenumber band and not a single depth or wavenumber. The scalogram does not provide a direct intuitive interpretation of depth or wavenumber. To interpret the scalogram, a number of approaches can be taken. The easiest step would be to stretch the scale to an equivalent wavenumber, depending on the scale-wavenumber mapping of the wavelet.

The centre wavenumber k_c of a signal s is defined as:

$$k_c = \frac{\int_0^\infty k |\tilde{S}(k)|^2 dk}{\int_0^\infty |\tilde{S}(k)|^2 dk}, \quad (6)$$

where $\tilde{S}(k)$ is the Fourier transform of a signal and k is wavenumber. In practice, the wavenumber maximizing the fast Fourier transform (FFT) of the wavelet modulus is chosen as its centre wavenumber $k_{c,w}$. The relationship between the scale and wavenumber is:

$$k_a = \frac{k_{c,w}}{a\Delta}, \quad (7)$$

where k_a is the wavelet pseudo-wavenumber corresponding to the scale a and the sampling interval Δ . $k_{c,w}$ is the centre wavenumber of an analysing wavelet. Once the mother wavelet is chosen, its centre wavenumber $k_{c,w}$ can be deter-

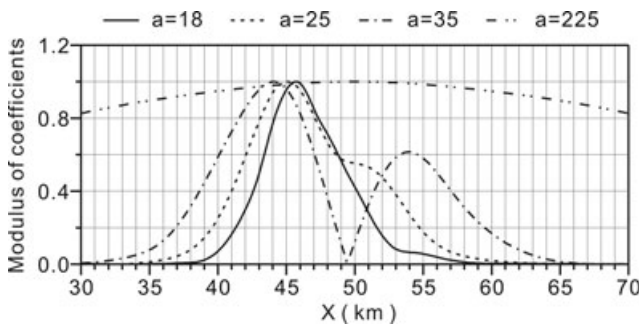


Figure 3 Modulus curves of complex coefficients computed from 1D complex wavelet transform at four scales (scale a : 18, 25, 35, 225; corresponding pseudo-wavenumber k_a : 0.2778, 0.2000, 0.1429, 0.0222 km^{-1}). The modulus has been normalized by its maximum value.

mined from equation (6). Then the scales in the scalogram can be transformed into pseudo-wavenumbers k_a by equation (7).

It is worth noting that the wavelet pseudo-wavenumber k_a and centre wavenumber $k_{c,w}$ are not equivalent to the

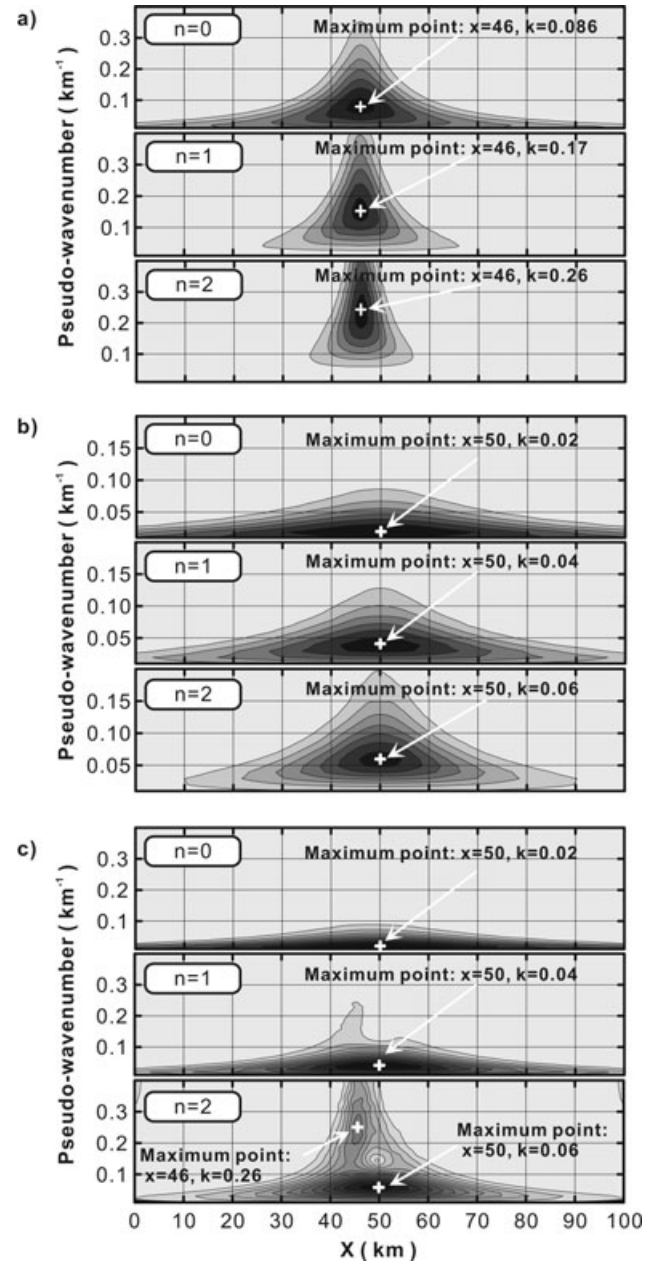


Figure 4 a) Scale-normalized scalograms of magnetic anomalies caused by single sphere 1 ($n = 0, 1, 2$), b) Scale-normalized scalograms of magnetic anomalies caused by single sphere 2 ($n = 0, 1, 2$) and c) by two spheres ($n = 0, 1, 2$). The complex Morlet wavelet (cmor1-1) is used as the analysing wavelet. Contours show the dimensionless modulus of wavelet coefficients. The modulus maxima are labelled as white plus.

centre wavenumber of magnetic anomalies (denoted as $k_{c,s}$). For profile (2D) data, the centre wavenumber can be determined from equation (6), whereas in the 3D case, the radial power spectrum (Spector 1970) has to be computed before we can get the centre wavenumber. The magnetic anomalies usually have higher centre wavenumbers at shallower buried depths and lower ones at deeper depths. Therefore, in the wavelet analysis of magnetic anomalies, smaller scales usually reflect shallower sources with higher wavenumbers and vice versa. In the following synthetic example, we will elaborate on the relationship between source depth and the pseudo-wavenumber corresponding to modulus maxima.

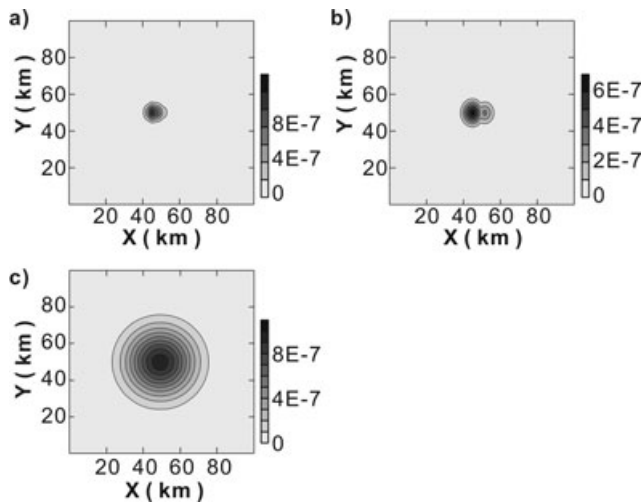


Figure 5 Scale-normalized wavelet spectrum slices ($n = 2$). a) $a = 19$, pseudo-wavenumber $k_a = 0.26 \text{ km}^{-1}$, b) $a = 28$, pseudo-wavenumber $k_a = 0.18 \text{ km}^{-1}$, c) $a = 83$, pseudo-wavenumber $k_a = 0.06 \text{ km}^{-1}$.

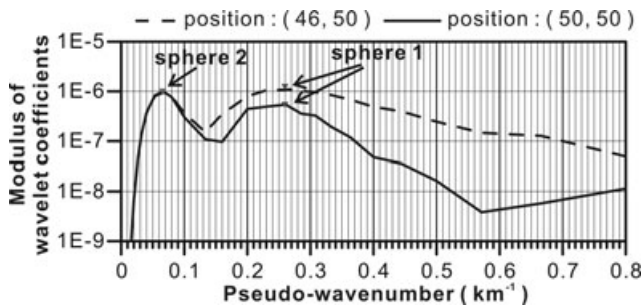


Figure 6 Modulus curves of wavelet coefficients versus pseudo-wavenumber. The dash line is the curve passing through the centre of sphere 1 ($x = 46 \text{ km}$, $y = 50 \text{ km}$) and the solid line is the curve passing through the centre of sphere 2 ($x = 50 \text{ km}$, $y = 50 \text{ km}$). Inverted triangles label the maximum locations.

A SYNTHETIC EXAMPLE

We consider the magnetic total field anomaly (Fig. 1c) produced by two spheres with magnetization 6 A/m. Sphere 1 has a radius of 0.5 km and is located at (46, 50, 3), while sphere 2 is located at (50, 50, 12) with a radius of 5 km. For simplification, the magnetic inclination is assumed to be 90° . The profiles are striking east-west, line spacing being 1 km and point spacing 0.2 km. There is a total of 101 lines in our model with 501 points in each line. It is hard to identify the magnetic anomalies of sphere 1 from the strong background field caused by sphere 2 in Fig. 1(c).

Table 1 Centre wavenumber $k_{c,s}$ of magnetic anomalies and pseudo-wavenumber $k_{a,2}^{(\max)}$ corresponding to modulus maxima of complex coefficients

Centre depth (km)	Centre wavenumber $k_{c,s} \text{ (km}^{-1}\text{)}$	Pseudo-wavenumber $k_{a,2}^{(\max)} \text{ (km}^{-1}\text{)}$
0.5	0.5988	1.5968
1	0.3033	0.7984
2	0.1519	0.3992
3	0.1013	0.2595
4	0.0759	0.1996
5	0.0607	0.1597
6	0.0506	0.1297
7	0.0433	0.1098
8	0.0379	0.0998
9	0.0337	0.0898
10	0.0303	0.0798
11	0.0275	0.0698
12	0.0252	0.0599

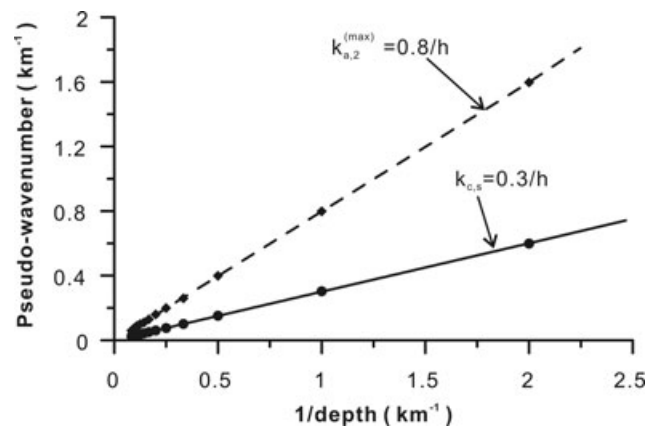


Figure 7 The linear relation between the sphere centre depth and centre wavenumber (solid line), dash line shows the relation between the centre depth and pseudo-wavenumber.

We then apply the 1D continuous wavelet transform on the magnetic anomalies of profile A-B to get their scalogram (modulus of wavelet coefficients computed by equation (1)). The complex Morlet wavelet (cmor1-1: bandwidth $k_b = 1 \text{ km}^{-1}$, centre wavenumber $k_{c,w}$ is 1 km^{-1}) is chosen as the analysing wavelet. Figure 2(a) shows magnetic anomalies caused by single sphere 1 on profile A-B. Judging from its scalogram, there is a modulus maximum (white plus) at the centre of sphere 1 ($x = 46 \text{ km}$). The pseudo-wavenumber k_a is about 0.086 km^{-1} (scale $a = 58$), which is close to the centre wavenumber of magnetic anomalies $k_{c,s}$ (0.1013 km^{-1}). The same is true for the magnetic anomalies caused by single sphere 2 and its scalogram (Fig. 2b). The modulus maximum also exists at the centre of sphere 2 ($x = 50 \text{ km}$). The corresponding pseudo-wavenumber k_a is about 0.022 km^{-1} (scale $a = 225$), very close to the centre wavenumber $k_{c,s}$ (0.0252 km^{-1}). Therefore, the modulus maxima in the complex wavelet scalogram are capable of identifying the source horizontal position. If the magnetic source is taken as a suite of dipoles, the source depths can be estimated from the above relationship between the centre wavenumber $k_{c,s}$ and the pseudo-wavenumber k_a , which corresponds to the modulus maximum.

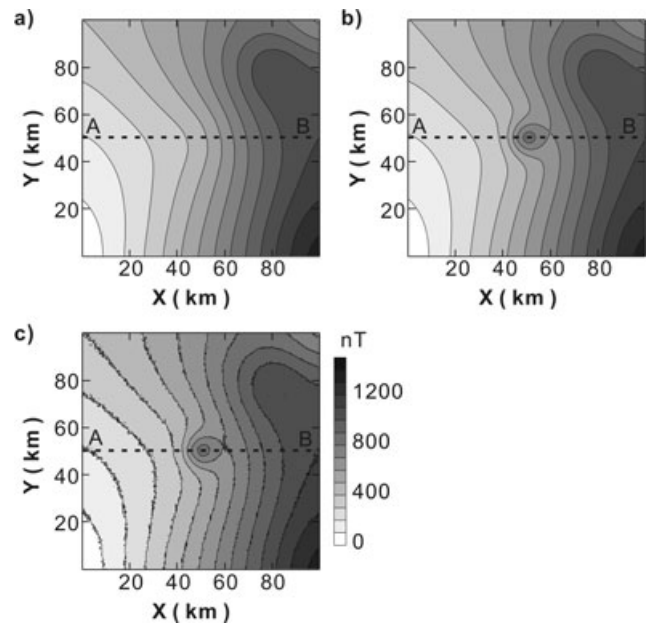


Figure 9 Total magnetic intensity anomalies (Fig. 1c) added with a background field and random noise. a) Background magnetic field, b) total magnetic intensity anomalies added with background field, c) total magnetic intensity anomalies added with background field and random noise, whose amplitude is 1% of the max amplitude of anomalies in Fig. 1(c).

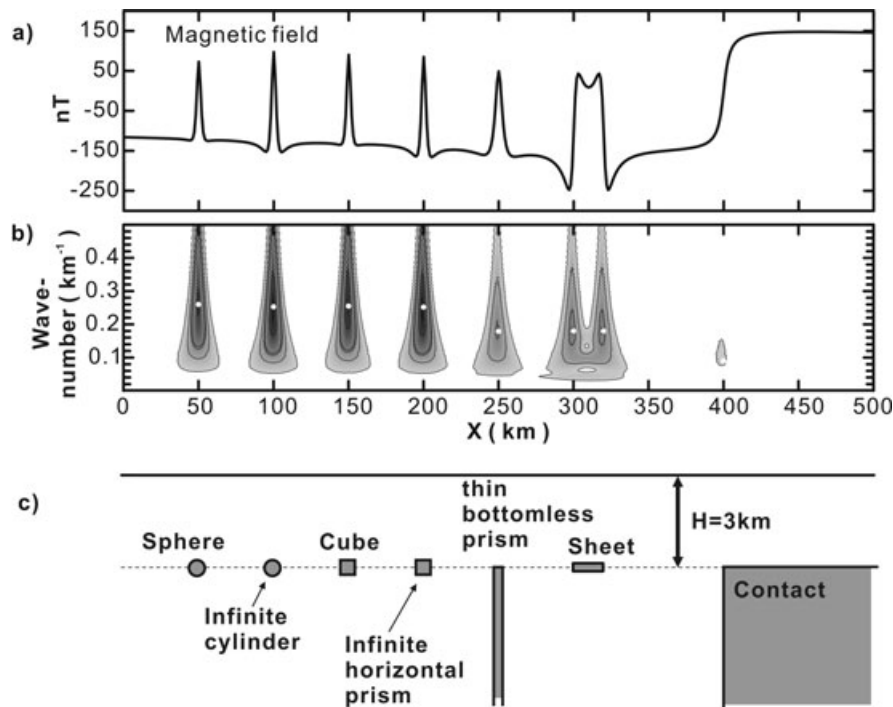


Figure 8 A synthetic model indicating source depth estimation errors of our method on seven simple bodies, including sphere, infinite horizontal cylinder, cube, infinite horizontal prism, thin bottomless prism, sheet and contact. a) Magnetic anomalies and b) their scalograms, white dots indicate maximum points, c) model geometries.

Now, let us take a look at the magnetic anomalies caused by sphere 1 and 2 and corresponding scalogram (Fig. 2c). An obvious maximum can be found, indicating the position of sphere 2. Sphere 1, whose total magnetic intensity amplitude is about 1/15 of sphere 2, is hard to identify from the scalogram. For a detailed description, we extracted the wavelet coefficients modulus at different scales (or pseudo-wavenumbers). Figure 3 shows the results (scale a : 18, 25, 35, 225; corresponding pseudo-wavenumber k_a : 0.2778, 0.2000, 0.1429, 0.0222 km^{-1} respectively). When $a = 18$ (solid line), the modulus of complex coefficients has a maximum at $x = 46$ km, coinciding well with the location of sphere 1 centre. As scales increase, two maxima can be seen and the influence of deeper sphere 2 becomes more significant. When $a = 225$ (dash-dot-dot line), there is only one maximum at $x = 50$ km, reflecting the location of sphere 2 centre. The pseudo-wavenumber ($k_a = 0.0222 \text{ km}^{-1}$) is also close to the centre wavenumber of magnetic anomalies caused by single sphere 2 (0.0252 km^{-1}). Therefore, the modulus maxima of complex coefficients at different scales can be adopted to identify adjacent geological bodies.

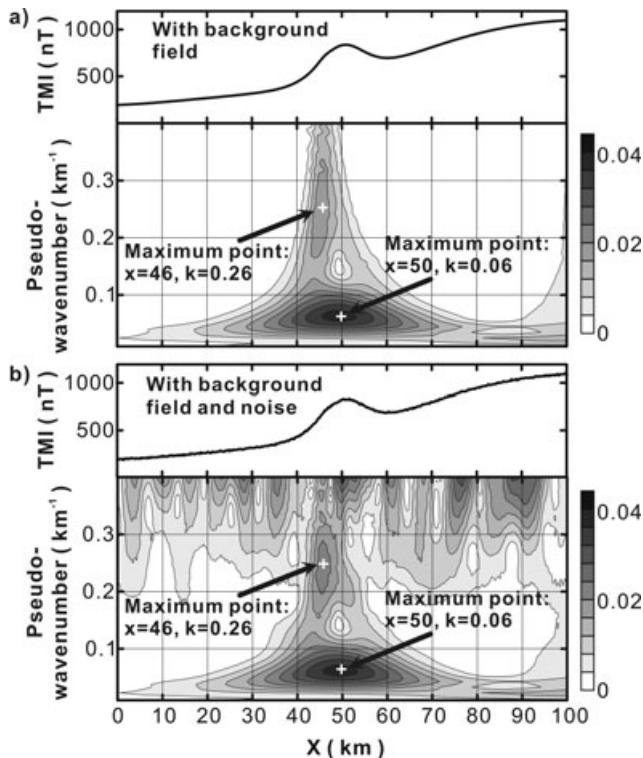


Figure 10 Magnetic anomalies in profile A-B and their scalograms. a) Magnetic anomalies (with background and noise-free) in profile A-B and their scalogram, b) magnetic anomalies (with background and noise) in profile A-B and corresponding scalogram.

Scale normalization

The synthetic example demonstrates that the magnetic anomalies of two adjacent bodies are not only superimposed on each other in space, they also have very close wavenumber constituents, which makes it a difficult task to separate them from

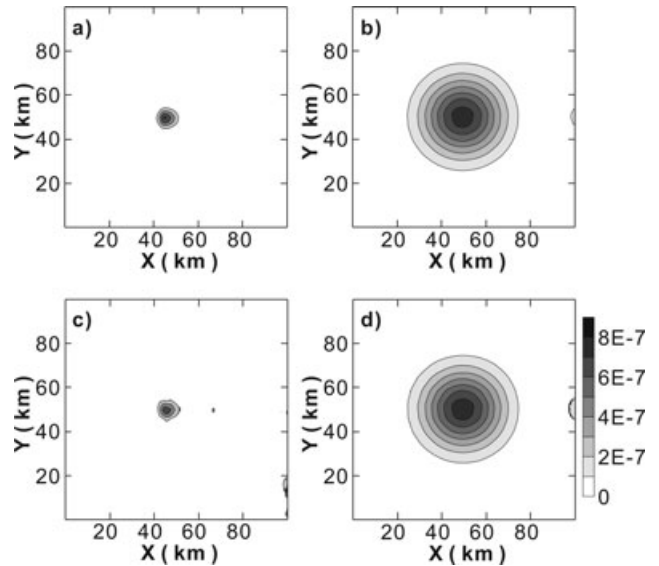


Figure 11 Wavelet spectrum slices at two scales. a–b) Wavelet spectrum slices of magnetic anomalies (Fig. 9b) at scale $a = 19$ and $a = 83$; c–d) wavelet spectrum slices of magnetic anomalies (Fig. 9c) at scale $a = 19$ and $a = 83$.

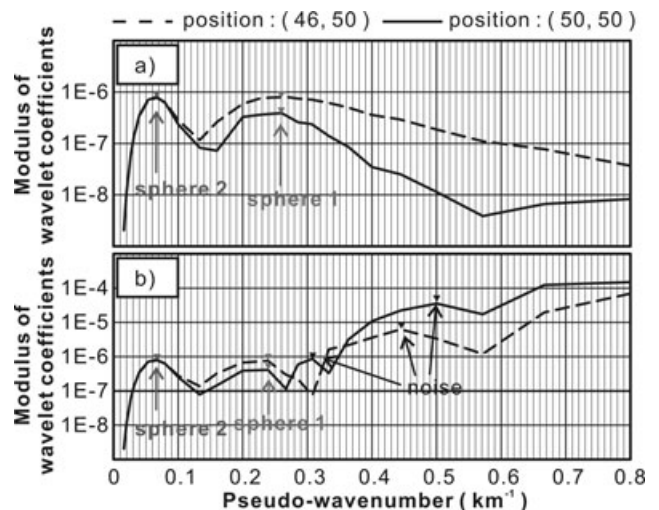


Figure 12 Modulus curves of complex coefficients versus pseudo-wavenumber passing through the centre of sphere 1 (dash line) and sphere 2 (solid line). a) Coefficient modulus curves versus pseudo-wavenumber for magnetic anomalies in Fig. 9(b) and b) for magnetic anomalies in Fig. 9(c). Inverted triangles label the maximum locations.

scalograms. For the purpose of enhancing wavenumber discrimination ability, we designed a scale normalization scheme by applying a power function of scale (a^{-n}) on the 1D continuous wavelet transform (equation (1)). Then the normalized 1D continuous wavelet transform can be expressed as

$$\tilde{S}'_W(a, b) = a^{-n} \int_{-\infty}^{\infty} s(x) \frac{1}{\sqrt{a}} \tilde{\psi} \left(\frac{x-b}{a} \right) dt, \quad (8)$$

where n is a positive constant. When $n = 0$, there is no scale normalization.

Figure 4(a) shows the recalculated scalograms of magnetic anomalies caused by single sphere 1 with scale normalization factor a^{-1} and a^{-2} . Compared with the non-normalized scalogram ($n = 0$), the modulus maxima migrate towards the high wavenumber, whose offsets are related with n . When

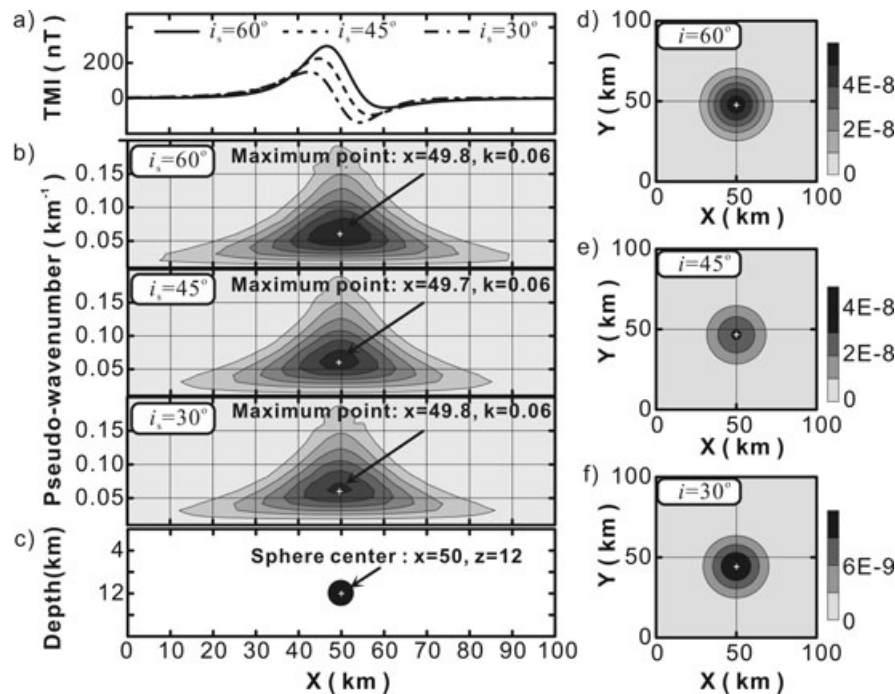


Figure 13 Magnetic anomalies and their scalograms in different magnetization inclination ($i_s = 30^\circ, 45^\circ, 60^\circ$). a) Magnetic anomalies of a sphere (50, 50, 12) magnetized in different inclinations ($i_s = 30^\circ, 45^\circ, 60^\circ$); b) Scalograms of total magnetic intensity anomalies in Fig. 13(a), white dots indicate maximum points; c) model geometry; d–f) spectrum slices at a certain pseudo-wavenumber ($k_a = 0.06 \text{ km}^{-1}$).

Table 2 The centre wavenumber $k_{c,s}$, pseudo-wavenumber k_a and the modulus maximum locations of complex coefficients in different magnetization inclination

Magnetization inclination ($^\circ$)	Sphere centre location (km)			Centre wavenumber (km^{-1})	Modulus maximum location		
	X	Y	Z		Pseudo-wavenumber (km^{-1})	X (km)	Y (km)
90	50	50	3	0.1013	0.26	50	50.0
60	50	50	3	0.1069	0.26	50	49.6
45	50	50	3	0.1145	0.26	50	49.2
30	50	50	3	0.1247	0.26	50	48.8
0	50	50	3	0.1351	0.26	50	50.0
90	50	50	12	0.0253	0.06	50	50.0
60	50	50	12	0.0267	0.06	50	48.2
45	50	50	12	0.0286	0.06	50	47.0
30	50	50	12	0.0312	0.06	50	44.8
0	50	50	12	0.0338	0.06	50	50.0

$n = 0$ (no normalization), the pseudo-wavenumber corresponding to the modulus maximum $k_{a,0}^{(\max)}$ is 0.086 km^{-1} . When $n = 1$, $k_{a,1}^{(\max)} \approx 2k_{a,0}^{(\max)} = 0.17 \text{ km}^{-1}$; $n = 2$, $k_{a,2}^{(\max)} \approx 3k_{a,0}^{(\max)} = 0.26 \text{ km}^{-1}$. The scale-normalized scalograms of magnetic anomalies of single sphere 2 have similar performance (shown in Fig. 4b). The scale-normalized scalograms (Fig. 4c) of our synthetic model (Fig. 1) indicate that, the modulus maxima have larger deviations in higher wavenumbers. Moreover, the maximum deviation discrepancies in higher and lower wavenumbers will become larger as n increases. Therefore, the scale-normalization is capable of discriminating modulus maxima in nearby wavenumbers. However, due to the calculation instability arising from large n values, we always set n between 0–2.5. In the following sections, we choose a^{-2} as our scale normalization factor.

The 2D continuous wavelet transform is applied on the magnetic anomalies (Fig. 1c) to get their wavelet spectrum. Figure 5(a–c) shows the spectrum slices at three scales. One local high anomaly can be seen in Fig. 5(a), representing shallower sphere 1; two local high anomalies in Fig. 5(b) reflect two spheres; while in Fig. 5(c) the local high anomaly is just the representation of sphere 2. In conclusion, the continuous wavelet spectrum slices under different scales are indicative for the magnetic source distribution in different depths.

For a more accurate description, we draw the wavelet coefficients modulus curve versus pseudo-wavenumber. Figure 6 shows the curves at two positions ($x = 46 \text{ km}$, $y = 50 \text{ km}$) and ($x = 50 \text{ km}$, $y = 50 \text{ km}$). Two modulus maxima can be seen on the dash curve, reflecting possible magnetic sources in two depths. One maximum at 0.26 km^{-1} reflects the position of sphere 1, which can be testified from Fig. 5(a). No maximum exists at position ($x = 46 \text{ km}$, $y = 50 \text{ km}$) on the wavelet spectrum slices at $k_a = 0.06 \text{ km}^{-1}$ (Fig. 5c), indicating that the modulus maximum at 0.06 km^{-1} (Fig. 6) is the reflection of nearby magnetic sources (sphere 2), whose centre is not just below the position ($x = 46 \text{ km}$, $y = 50 \text{ km}$). Similar analysis can also be applied to the solid curve (Fig. 6) to determine the source distribution.

Discussion on the relationship between depth and pseudo-wavenumber

Total magnetic intensity anomalies of single sphere (radius 0.5 km , vertically magnetized with a magnetization of 6 A/m) buried at different depths and their scale-normalized complex coefficients are calculated (mother wavelet: complex Morlet wavelet, $k_c = k_b = 1 \text{ km}^{-1}$, scale-normalization factor is a^{-2}). The centre wavenumbers $k_{c,s}$ of magnetic anomalies along

profile A-B and the pseudo-wavenumber $k_{a,2}^{(\max)}$ corresponding to every modulus maximum are displayed in Table 1.

Figure 7 indicates that a linear relationship exists between the centre depth b and the centre wavenumber $k_{c,s}$, $k_{c,s} \approx 0.3/b$. Meanwhile, the pseudo-wavenumber $k_{a,2}^{(\max)}$ is also varied linearly with centre depth b , $k_{a,2}^{(\max)} \approx 0.8/b$. In a generalized sense, we can obtain

$$k_{a,n}^{(\max)} \approx 0.8(n+1)/3b, \quad (9)$$

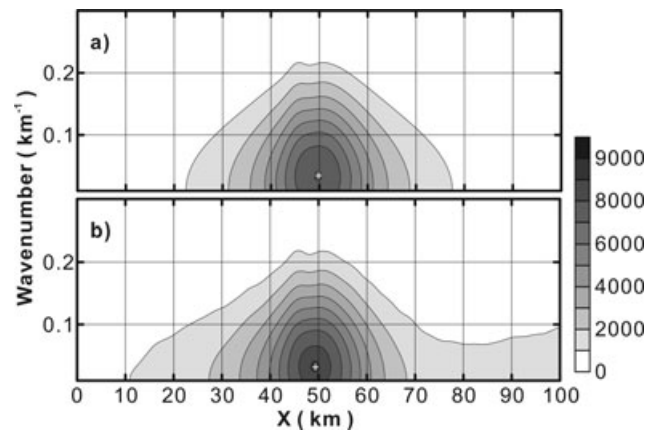


Figure 14 The short-time Fourier transform on the magnetic anomalies of profile A-B. a) Spectrogram of the magnetic anomalies (Fig. 2c) without background field and random noise, b) spectrogram of the magnetic anomalies with background field and random noise (Fig. 10b). A 12-km-long Hanning window is used.

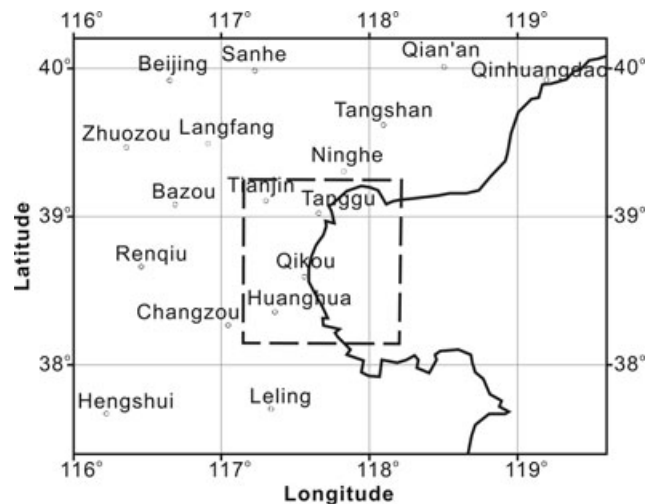


Figure 15 Location map of our study area. Dashed square delineates our study area and the black solid line outlines the coast line of the Bohai Bay.

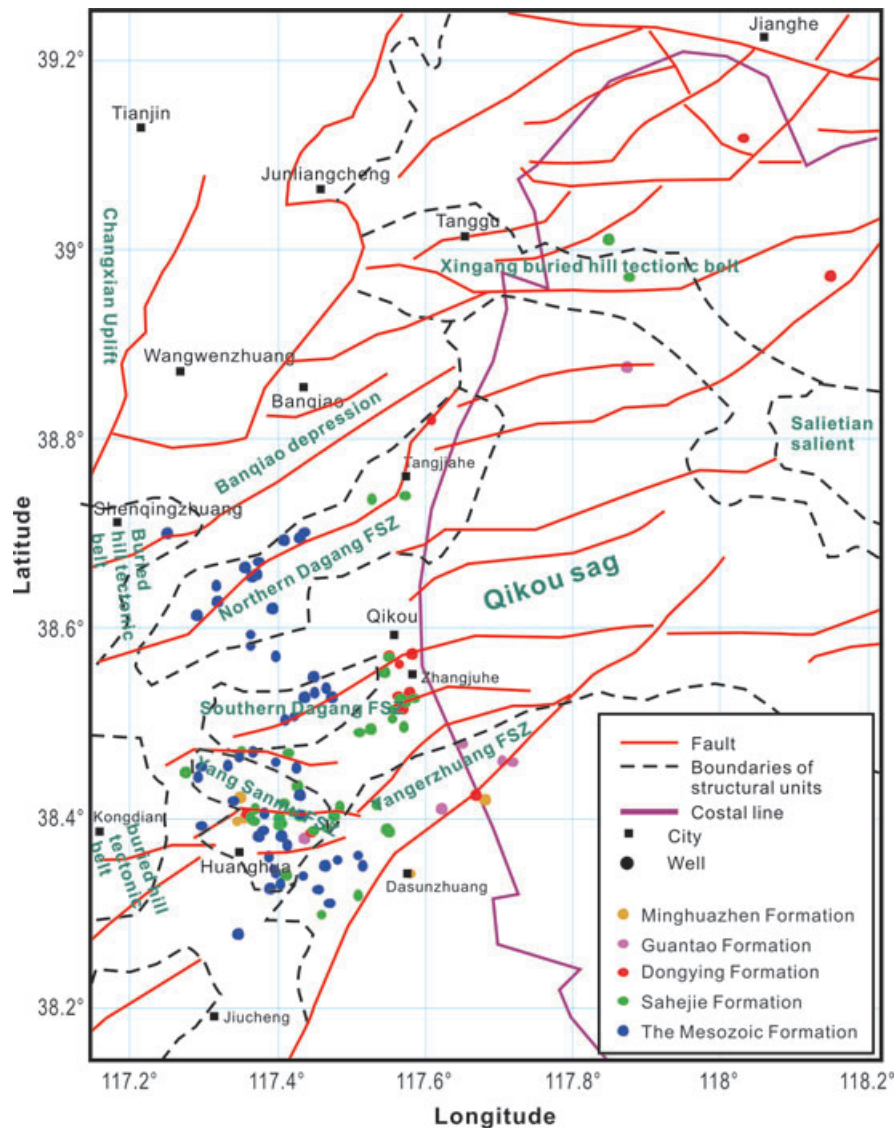


Figure 16 A simplified geological map with well data.

where n is a positive constant and $k_{a,n}^{(\max)}$ is the pseudo-wavenumber corresponding to modulus maximum after the scale normalization was applied.

When magnetic sources are far away from the observe plane, they are usually assumed as spheres. Then the apparent source depths can be estimated from the pseudo-wavenumbers of modulus maxima by equation (9). Often, other simple sources, such as line of dipoles, sheet or contact, are also widely used. Therefore, it is necessary for us to check our method with sources other than spherical. Figure 8(c) shows our models, which are composed of seven simple bodies (sphere, infinite horizontal cylinder, cube, infinite horizontal prism, thin bottomless prism, sheet, contact) buried

at depth of 3 km. The model geometries are: the radius of the sphere and infinite horizontal cylinder is 0.5 km, the side length of the cube and infinite horizontal prism is 1 km, the width of the thin bottomless prism is 1 km and the sheet is 20 km wide. Fig. 8(a,b) shows the magnetic anomalies and their scalograms. White dots in Fig. 8(b) indicate the maximum points, coinciding well with the location of model centres or boundaries. The pseudo-wavenumbers corresponding to maximum points of the thin bottomless prism and sheet are about 2/3 of that of the sphere, infinite horizontal cylinder, cube and infinite horizontal prism, which are almost equal. The contact has the smallest pseudo-wavenumber, which is about 1/3 of that of the sphere.

Table 3 Statistics on the susceptibility of volcanic rocks from the Huanghua depression and adjacent region

Stratum	Lithology	Susceptibility ($\times 10^{-5}$ SI)		
		Min value	Max value	Mean value
E _{1s}	Mudstone, sandstone	0	13	5
	Basalt	200	2500	1600
	Basaltic andesite	2000	4000	2500
E _{2-4s}	Basalt, andesite	300	3500	2200
	Diabase	500	3800	1939
	Mudstone, sandstone	0	25	6.4
	Clastic mudstone	0	48	4.8
E _k	Sandstone	0	35	8
	Mudstone	10	120	42
	Basalt	600	2200	939
Mz	Pyroclastic rock	40	350	170
	Andesite	45	3500	1500
	Sandstone, mudstone	0	80	13
C-P	Mudstone, sandstone and limestone	20	250	83
	Mudstone	5	180	24
€-O	Limestone	0	13	5
	Limestone	0	0	0
Ar—Pt	Granitic gneiss	400	2500	970
	Amphibolite	800	8500	4770
	Biotite gneiss	150	2000	520

Therefore, errors arise when we still use equation (9) to estimate depths of the thin bottomless prism, sheet and contact. The synthetic model indicates that the pseudo-wavenumber corresponding to modulus maximum is related to source types. For point of mass or line of mass, such as sphere, infinite horizontal cylinder, cube and infinite horizontal prism, equation (9) still validates. Whereas for thin bottomless prism or sheet, equation (9) should be modified as: $\frac{2}{3}k_{a,n}^{(\max)} \approx 0.8(n+1)/3h$. And for contact of infinite depth extent, equation (9) should be modified into: $\frac{1}{3}k_{a,n}^{(\max)} \approx 0.8(n+1)/3h$. In conclusion, it is advisable to acquire the parameter characteristic of the source type (Reid *et al.* 1990; Martelet *et al.* 2001; Fedi 2007) before depth estimation.

In the following, some tests on the effects of prior model and noise on the source identification are made.

The effects of background magnetic field and random noise

A background magnetic field (Fig. 9a) and random noise are added into the total magnetic intensity anomalies (Fig. 1c), forming a more realistic example (Fig. 9c). Figure 10(a,b) shows magnetic anomalies (Fig. 9b,c) in profile A-B and their

scalograms. Figure 11 shows wavelet spectrum slices of magnetic anomalies in Fig. 9(b,c) at two scales ($a = 19$ and 83). At last, the wavelet coefficients modulus curve versus pseudo-wavenumber (Fig. 12) at the centre of two spheres ($x = 46$ km, $y = 50$ km) and ($x = 50$ km, $y = 50$ km) are drawn for a detailed description.

Based on similar analysis as in above sections, we believe that the regional trends have little effect on our method, while the influence of random noise is mainly imposed on shallower sources.

The effects of magnetization direction

In the above theoretical modelling, the modulus maxima of complex coefficients are used to locate magnetic sources being vertically magnetized. But in most cases, the magnetic bodies are always in oblique magnetization, with a magnetization inclination $I \neq 90^\circ$.

Figure 13(a–c) shows magnetic anomalies of a spherical model and their scalograms in three magnetization inclinations. In Fig. 13(b), pseudo-wavenumbers k_a remain

unchanged for different magnetization inclinations, indicating no effects of magnetization inclination on the source depth estimation.

Table 2 shows that the magnetization inclination has relatively stronger effects on the centre wavenumber k_{cs} than on the pseudo-wavenumber k_a . And the situation becomes more serious for deeper sources. Therefore, magnetic anomalies have to be reduced to the pole before the continuous wavelet transform is applied. It is noteworthy that errors will arise if the magnetization direction is not correct while performing reduction to the pole. The output anomaly will be distorted and this may even cause a horizontal source mislocation.

Short-time Fourier transform

We can include the time (or space) dependence by windowing the signal (i.e., taking short segments of the signal) and then performing the Fourier transform on the windowed data to obtain local frequency information. Such an approach of time-frequency analysis is called the short-time Fourier transform and the time-frequency map is called a spectrogram (Cohen 1995).

We show spectrograms computed for magnetic anomalies of profile A-B with none and having background field and random noise in Fig. 14. A 12-km-long Hanning window was used for computation. Note in the spectrograms that the low wavenumbers are well resolved and the high wavenumbers are either poorly resolved or not visible at all. The reason is that the wavenumber resolution is fixed by the pre-selected window length, which is recognized as the fundamental problem of the short-time Fourier transform in the spectral analysis of a non-stationary signal. By comparing Fig. 14 with Figs 4(c) and 10(b), it is evident that the wavelet analysis is more effective than short-time Fourier transform.

APPLICATION OF THE CONTINUOUS WAVELET TRANSFORM METHOD TO FIELD DATA

The dashed square in Fig. 15 indicates our study area. Tectonically speaking, our study area is located in the north centre of the Huanghua depression in the Bohai Bay basin, eastern China. The tectonic framework of this area (Fig. 16) can be described as three structural fault zones, two secondary sags and three slopes. Specifically speaking, three structural fault zones (FSZ) refer to the Northern Dagang FSZ, Southern Dagang FSZ and Yangerzhuang FSZ from

north to south. Divided by the Southern Dagang FSZ, the Qikou sag was separated into two secondary sags, the north Qikou sag and south Qikou sag. Both sags have dustpan-like, asymmetric structures. In the transition region between sags and salients, three gentle slopes are developed (Lang 2008).

The magmatism of this area has been in active condition since the Eocene stage, forming various types of volcanic

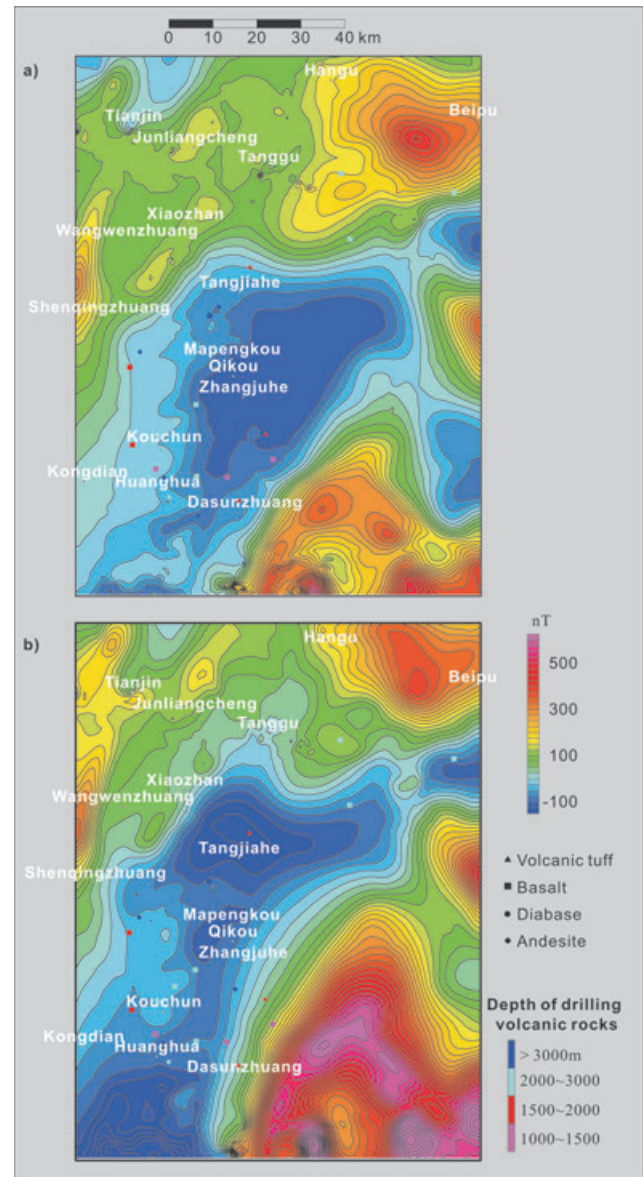


Figure 17 a) 1:200,000 aeromagnetic data of our study area, b) RTP aeromagnetic anomalies of our study area. Coloured symbols stand for locations of drilling holes encountered with volcanic rocks at different depths. White dots show place names.

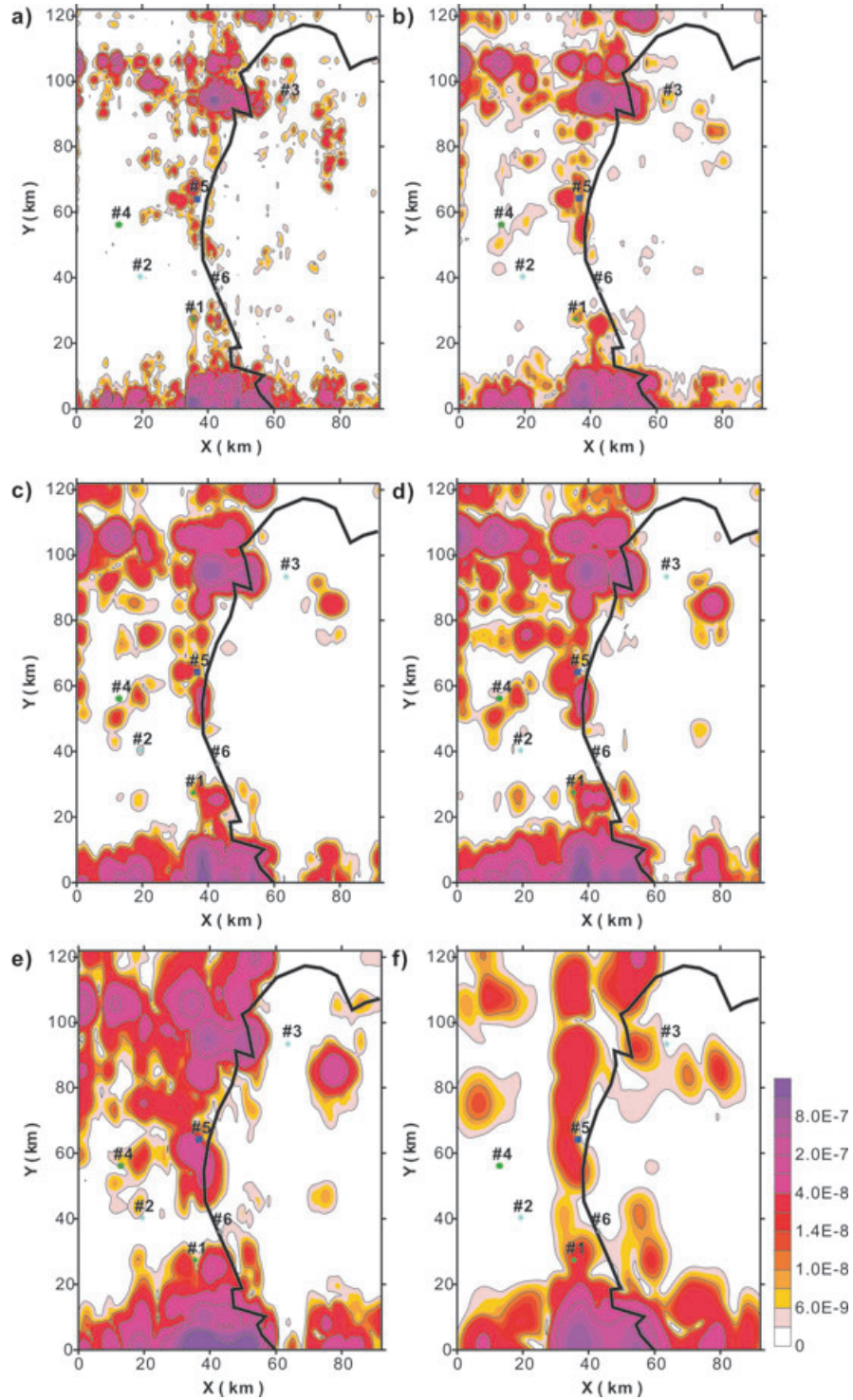


Figure 18 Wavelet spectrum slices under different scales. a) $a = 8.75$ ($k_a = 0.57 \text{ km}^{-1}$, $h \approx 1.4 \text{ km}$), b) $a = 12.5$ ($k_a = 0.4 \text{ km}^{-1}$, $h \approx 2.0 \text{ km}$), c) $a = 15$ ($k_a = 0.33 \text{ km}^{-1}$, $h \approx 2.4 \text{ km}$), d) $a = 17.2$ ($k_a = 0.29 \text{ km}^{-1}$, $h \approx 2.8 \text{ km}$), e) $a = 21.75$ ($k_a = 0.23 \text{ km}^{-1}$, $h \approx 3.5 \text{ km}$), f) $a = 38.5$ ($k_a = 0.13 \text{ km}^{-1}$, $h \approx 6.0 \text{ km}$).

rocks, such as basalts, diabbases, andesites and volcanic tuffs. According to the well logs, the Meso-Cenozoic volcanic rocks have been encountered in the Minghuazhen formation (Nm) and Guantao formation (Ng) of Neogene period, the Dongying formation (Ed) and Sahejie formation (Es) of Paleogene period and the Mesozoic strata. Up to now, seven volcanic reservoirs and two oilfields producing ten million tons per year have been revealed by integrated geophysical and geological study (Lang 2008; Zhang *et al.* 2008).

Most volcanic rocks show ferromagnetism due to their content of ferromagnetic minerals. Table 3 shows the susceptibility of volcanic rocks from the Huanghua depression and adjacent region. The susceptibilities of basin sediments (mudstone and sandstone) vary between 0×10^{-5} SI and 83×10^{-5} SI, while igneous rocks have stronger magnetism, whose susceptibilities vary between 200×10^{-5} SI and 4000×10^{-5} SI. Therefore, they usually have stronger magnetic responses than other rocks, forming the basis of using aeromagnetic data to delineate the distribution of volcanic rocks.

The 1:200,000 aeromagnetic data (Fig. 17a) were collected at a flight altitude of 90 m in north-south orientation, the distance of flight lines is 2 km with point spacing 60 m. The grid spacing is 1 km. The reduction to the pole (RTP) magnetic anomalies are shown in Fig. 17(b), with the magnetic inclination 56.01° and magnetic declination -6.01° . Triangles, circles, squares and diamonds represent the well locations drilling through volcanic tuffs, diabbases, basalts and andesites and with four different colours indicating the depth at which these volcanic rocks were encountered. No obvious relation exists between the aeromagnetic anomalies and the drilling holes encountered with volcanic rocks (as shown in Fig. 17b). Therefore, it is hard to identify volcanic rocks directly from the RTP aeromagnetic data.

According to exploration experience, the volcanic rocks in our study area are mainly buried at a depth of 1–3.5 km, whose corresponding pseudo-wavenumber is about $0.23\text{--}0.80 \text{ km}^{-1}$ (equation (9)). For a detailed description of volcanic rocks, we applied the continuous wavelet transform on the RTP aeromagnetic data to get the wavelet spectrum slices at six scales. Results are shown in Fig. 18(a–f).

It is hard for us to analyse all the drilling holes, for simplification, we chose six ones for testifying the effectiveness of our methodology. Figure 19(a–f) shows the modulus curves of complex coefficients versus pseudo-wavenumber for six drilling holes. We start our analysis from drilling hole #1, which encountered basalts at the depth of 1.4 km and 2 km (Table 4). Four maxima can be seen in Fig. 19(a). Two of them are in good accordance with drilling results and the

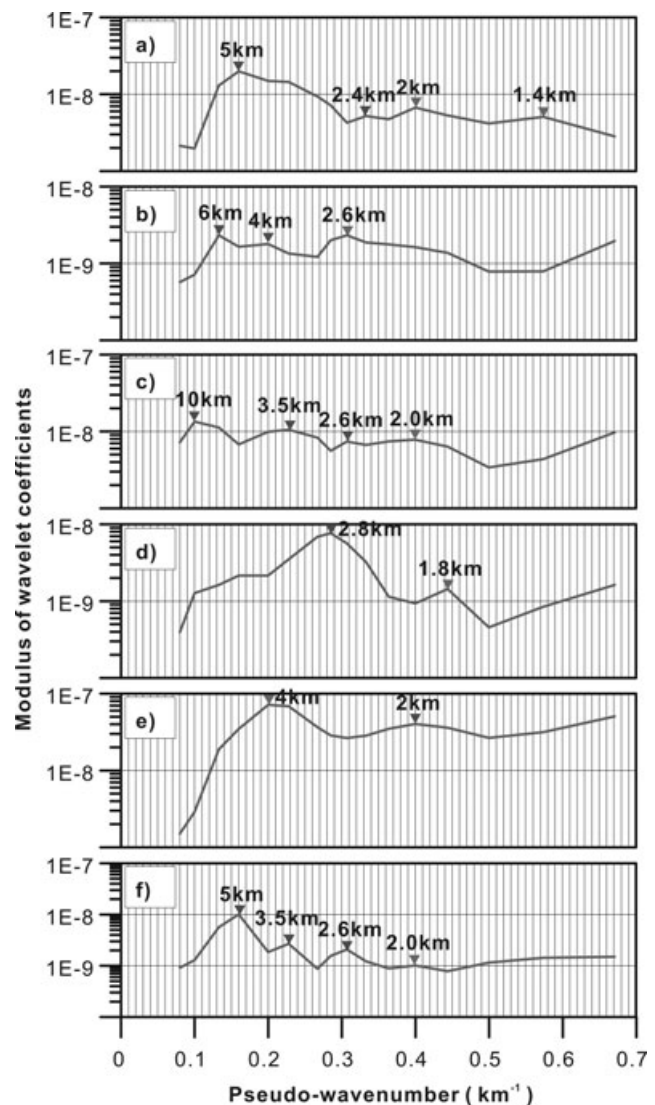


Figure 19 Modulus curves of wavelet coefficients versus pseudo-wavenumber of six drilling holes. a) Drill hole #1, four maxima at pseudo-wavenumber: 0.57, 0.4, 0.33, 0.16 km^{-1} ; b) drill hole #2, three maxima at pseudo-wavenumber: 0.31, 0.20, 0.13 km^{-1} ; c) drill hole #3, four maxima at pseudo-wavenumber: 0.4, 0.31, 0.23, 0.08 km^{-1} ; d) drill hole #4, two maxima at pseudo-wavenumber: 0.44, 0.29 km^{-1} ; e) drill hole #5, two maxima at pseudo-wavenumber: 0.40, 0.20 km^{-1} ; f) drill hole #6, four maxima at pseudo-wavenumber: 0.4, 0.31, 0.23, 0.16 km^{-1} . Inverted triangles label maximum points; estimated depths are indicated on the curves.

other ones are located at the border of local high anomalies in Figs 18(c) and 18(f). We infer that there are two possibilities: one is the existence of andesites or volcanic tuffs with moderate and weak magnetism; the other is the response of

Table 4 Statistics on volcanic rocks encountered by six drilling holes

No.	Depth (m)	Lithology	Layers	Total thickness (m)	Magnetism
#1	1400–1500	Basalts	2	39	strong
	1800–2000	Basalts	4	8	strong
#2	2500–2700	Basalts	28	88	strong
#3	2000–2350	Basalts, volcanic tuffs	11	235	Strong
#4	1850–2000	Andesites, volcanic tuffs	4	71	moderate
#5	3200–3500	Diabases	6	182	strong
#6	1897–1899	Volcanic tuffs	1	2	weak

nearby volcanic rocks. As for drill hole #2, one maximum coincides with drilling results (Table 4), falling into the local high anomaly in Fig. 18(c). The other two are not located at local high anomalies in Fig. 18(e,f). Perhaps they are the reflection of nearby volcanic rocks. Similar analysis could be carried out on other drill holes.

The faults are critical in controlling the distribution of volcanic rocks. The northern shallow volcanic rocks are mainly scattered along a NWW fault and other shallow ones distributed along N-E faults. As depth increases, the volcanic rocks eventually distribute along near N-S oriented faults (Fig. 18f).

CONCLUSIONS

We have successfully used the continuous wavelet transform decomposition method to map the distribution of volcanic rocks using aeromagnetic data. Theoretical modelling indicates that, the weak magnetic anomalies concealed by strong background field can be identified by the scale normalized complex wavelet transform. If magnetic sources are assumed as the combination of spheres, we can deduce the source distribution by the spectrum slices in different scales and the average source depth can be estimated from the modulus maximum of complex coefficients based on the linear relationship between the depth and the wavelet pseudo-wavenumber. Our study confirms the efficiency of the continuous wavelet transform method for the detection of wavenumber-dependent anomalies that may be due to volcanic rocks and in this way, it can be used in the early stages of hydrocarbon exploration in volcanic basins.

The wavelet technique is aimed at analysing both the geometry and locations of the sources of aeromagnetic data. This can also be applied to other potential fields, such as the gravity data. Despite the nonuniqueness of potential data interpreta-

tion, it provides a relatively inexpensive method to quickly assess large tracts of data.

ACKNOWLEDGEMENTS

This work was supported by a grant from the PhD Programs Foundation of the Ministry of Education of China for Distinguished Young Scholars (No. 200804911523) and by the Research Foundation for Outstanding Young Teachers, China University of Geosciences (No.CUGQNL0726). The Dagang Oilfield Company of China National Petroleum Corp. is gratefully acknowledged for supplying the geophysical data. We are very grateful to the reviewers, including Dr Giovanni Florio and another anonymous reviewer and to the deputy editor, Dr Alan Reid for their constructive comments and suggestions, which have greatly improved the original version of the manuscript. We also thank Bouasla Said for helpful suggestions on English writing.

REFERENCES

- Bhattacharyya B.K. and Leu L. 1975. Spectral analysis of gravity and magnetic anomalies due to two-dimensional structure. *Geophysics* **40**, 993–1013.
- Castagna J.P. and Sun S. 2006. Comparison of spectral decomposition methods. *First Break* **24**, 75–79.
- Castagna J.P., Sun S. and Siegfried R. 2003. Instantaneous spectral analysis: Detection of low-frequency shadows associated with hydrocarbons. *The Leading Edge* **22**, 127–129.
- Cohen L. 1995. *Time-frequency Analysis*. Prentice Hall. ISBN 0135945321.
- Daubechies I. 1987. Orthonormal bases of wavelets with finite support-connection with discrete filters. In: *Wavelets, Time-frequency Methods and Phase-space* (eds J.M. Combes, A. Grossmann and P. Tchamitchian), pp. 38–66. Springer Verlag. ISBN 0387530142.
- Emeleus C.H. and B.R. Bell. 2005. British regional geology. In: *The Palaeogene Volcanic District of Scotland*, 4th edn. British Geological Survey.

- Fedi M. 2007. DEXP: A fast method to determine the depth and the structural index of potential fields sources. *Geophysics* **72**, I1–I11.
- Fedi M. and Quarta T. 1998. Wavelet analysis for the regional-residual and local separation of potential field anomalies. *Geophysical Prospecting* **46**, 507–525.
- Gabor D. 1946. Theory of communications. *Journal of the Institute of Electrical Engineers* **93**, 429–457.
- Hardy H.H., Richard A.B. and Gaston J.D. 2003. Frequency estimates of seismic traces. *Geophysics* **68**, 370–380.
- Hornby P., Boschetti F. and Horowitz F.G. 1999. Analysis of potential field data in the wavelet domain. *Geophysical Journal International* **137**, 175–196.
- Hunter B.E. and Davies D.K. 1979. Distribution of volcanic sediments in the Gulf coastal province – Significance to petroleum geology. *Transactions, Gulf Coast Association of Geological Societies* **29**, 147–155.
- Kazemeini H., Juhlin C., Zinck-Jorgensen K. and Norden B. 2007. Application of the continuous wavelet transform decomposition to channel deposits and gas detection at Ketzin, Germany. 69th EAGE meeting, London, UK, Expanded Abstracts.
- Kazemeini S.H., Juhlin C., Zinck-Jorgensen K. and Norden B. 2009. Application of the continuous wavelet transform on seismic data for mapping of channel deposits and gas detection at the CO₂SINK site, Ketzin, Germany. *Geophysical Prospecting* **57**, 111–123.
- Lang J. 2008. *Research on exploration and estimation technologies for subtle reservoir in slope of Qikou Sag*. PhD thesis, China University of Geosciences (in Chinese).
- Luo J., Zhang C. and Qu Z. 1999. Volcanic reservoir rocks: A case study of the cretaceous fenghuadian suite, Huanghua Basin, Eastern China. *Journal of Petroleum Geology* **22**, 397–415.
- Mallat S. 1999. *A Wavelet Tour of Signal Processing*. Academic Press. ISBN 012466606X.
- Martelet G., Sailhac P., Moreau F. and Diament M. 2001. Characterisation of geological boundaries using 1-D wavelet transform on gravity data: Theory and application to the Himalayas. *Geophysics* **66**, 1116–1129.
- Mitsuhata Y., Matsuo K. and Minegishi M. 1999. Magnetotelluric survey for exploration of a volcanic rock reservoir in the Yurihara oil and gas field, Japan. *Geophysical Prospecting* **47**, 195–218.
- Moreau F., Gibert D., Holschneider M. and Saracco G. 1997. Wavelet analysis of potential fields. *Inverse Problems* **13**, 165–178.
- Moreau F., Gibert D., Holschneider M. and Saracco G. 1999. Identification of sources of potential fields with the continuous wavelet transform: Basic theory. *Journal of Geophysical Research* **104**, 5003–5013.
- Partyka G.J., Gridley J. and Lopez J. 1999. Interpretational applications of spectral decomposition in reservoir characterization. *The Leading Edge* **18**, 353–360.
- Peyton L., Bottjer R. and Partyka G. 1998. Interpretation of incised valleys using new 3-D seismic techniques: A case history using spectral decomposition and coherency. *The Leading Edge* **17**, 1294–1298.
- Reid A.B., Allsop J.M., Granser H., Millett A.J. and Somerton I.W. 1990. Magnetic interpretation in three dimensions using Euler deconvolution. *Geophysics* **55**, 80–91.
- Rohrman M. 2007. Prospectivity of volcanic basins: Trap delineation and acreage de-risking. *AAPG Bulletin* **91**, 915–939.
- Sailhac P., Galdeano A., Gibert D., Moreau F. and Delor C. 2000. Identification of sources of potential fields with the continuous wavelet transform: Complex wavelet and application to aeromagnetic profiles in French Guiana. *Journal of Geophysical Research* **105**, 19,455–19,475.
- Schutter S.R. 2003. Occurrences of hydrocarbons in and around igneous rocks. In: *Hydrocarbons in Crystalline Rocks* (eds N. Petford and K.J.W. McCaffrey), pp. 35–68. Geological Society of London. ISBN 1862391378.
- Sinha S., Routh P.S., Anno P.D. and Castagna J.P. 2005. Spectral decomposition of seismic data with continuous-wavelet transforms. *Geophysics* **70**, 19–25.
- Spector A. and F.S. Grant. 1970. Statistical models for interpreting aeromagnetic data. *Geophysics* **35**, 293–302.
- Zhang T., Zhang M., Bai B., Wang X. and Li L. 1999. Origin and accumulation of carbon dioxide in the Huanghua depression, Bohai Bay Basin, China. *AAPG Bulletin* **92**, 341–358.